

₁ Physics-Infused Reduced-Order Modeling for Analysis of
₂ Ablating Hypersonic Thermal Protection Systems

₃

₄ November 11, 2025

₅ **Abstract**

This work presents a *physics-infused reduced-order modeling* (PIROM) framework towards the design, analysis, and optimization of non-decomposing ablating hypersonic thermal protection systems (TPS). It is demonstrated via the modeling of transient thermo-ablative behavior of non-decomposing multi-layered hypersonic TPS. The PIROM architecture integrates a reduced-physics backbone, based on the lumped-capacitance model (LCM), with data-driven correction dynamics formulated via a coarse-graining approach rooted in the Mori-Zwanzig formalism. The LCM is coupled to a surface velocity model (SVM) to capture the recession of the ablating TPS as a function of the surface temperature. While the LCM and SVM capture the dominant physics of the ablating TPS response, the correction terms compensate for residual dynamics arising from higher-order non-linear interactions and heterogeneities across material layers. The PIROM consistently achieves errors below 1% for a wide range of extrapolative settings of design parameters involving time-and-space varying boundary conditions and SVM models, and improves by $x\%$ over the LCM alone. Moreover, the PIROM delivers online evaluations that are two orders of magnitude faster than the full-order model (FOM). These results demonstrate that PIRO effectively reconciles the trade-offs between accuracy, generalizability, and efficiency, providing a promising framework for optimizing multi-physical dynamical systems, such as TPS under diverse operating conditions.

₂₅ **1 Introduction**

₂₆ At hypersonic speeds, aerospace vehicles experience extreme aero-thermo-dynamic environments that require specialized thermal protection systems (TPS) to shield internal sub-
₂₇ structures, electronics, and possibly crew members from the intense aerodynamic heating.
₂₈

29 The TPS is often composed of ablating materials – a high-temperature capable fibrous
30 material injected with a resin that fills the pore network and strengthens the composite
31 [Amar2016](#). The TPS design promotes the exchange of mass through thermal and
32 chemical reactions (i.e., pyrolysis), effectively mitigating heat transfer to the sub-structures.

33 As a result, accurate prediction for the ablating TPS response under extreme hyper-
34 sonic heating becomes fundamental to ensuring survivability, performance, and safety of
35 hypersonic vehicles. Not only is it necessary to assess the performance of the thermal man-
36 agement systems, but also the shape changes of the vehicle’s outer surface induced by the
37 ablating material, and its impact on the aerodynamics, structural integrity, and controlla-
38 bility. Nonetheless, high-fidelity simulations of ablating TPS remains a formidable challenge
39 both theoretically and computationally.

40 Unfortunately, high-fidelity simulations of ablating TPS remains a formidable challenge
41 both theoretically and computationally.

42 On the theoretical side, the thermo-chemical reactions, coupled with the irregular pore
43 network structure, translate into simplifying assumptions to reduce non-linearities, and make
44 the resulting equations more amenable for engineering application and design analysis [x](#).
45 For instance, one of the most notable codes is the one-dimensional [CMA](#) code that was
46 developed by Aerotherm Corporation in the 1960s [Howard2015](#). Despite its practical use
47 in...

48 Another example is the CHarring Ablator Response (CHAR) ablation code, which ignores
49 elemental decompositions of the pyrolyzing gases, assumes the gases to be a mixture of perfect
50 gases in thermal equilibrium, and assumes no reaction or condensation with the porous
51 network [1].

52 [theoretically:](#)

53 [computationally:](#)

54 2 Modeling of Ablating Thermal Protection Systems

55 This section presents the problem of modeling a non-decomposing ablating TPS subjected to
56 extreme hypersonic heating. Two different but mathematically connected solution strategies
57 are provided: (1) a high-fidelity full-order model (FOM) based on a finite element method
58 (FEM), and (2) a low-fidelity reduced-physics model (RPM) based on a lumped capacitance
59 model (LCM) and a one-dimensional surface velocity model (SVM). The FOM is compu-
60 tationally expensive but provides the highest fidelity, while the RPM is computationally
61 efficeint but has low predictive fidelity; both models are amenable to high-dimensional de-
62 sign variables. The RPM is used in the subsequent sections for deriving the PIROM.

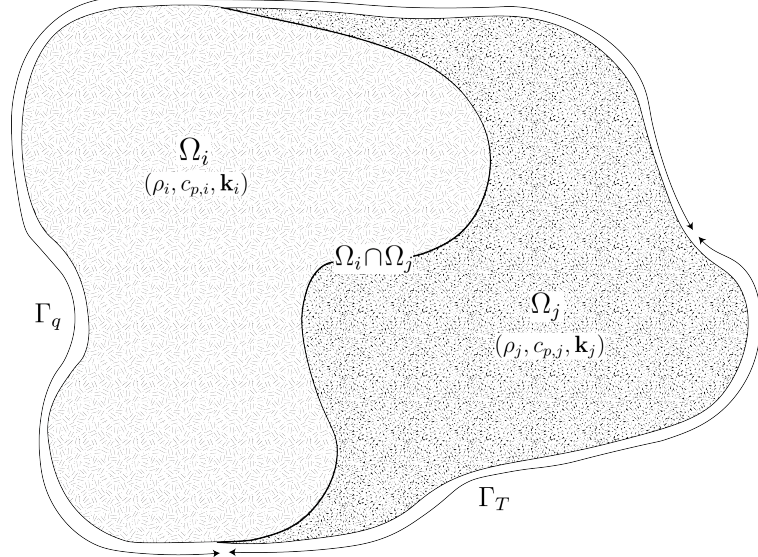


Figure 1: General domain Ω with prescribed Neumann and Dirichlet boundary conditions on Γ_q and Γ_T . Mesh displacement $w(x, t)$ occurs on the Γ_q boundary.

63 2.1 Governing Equations

64 The multi-physics for a non-decomposing ablating TPS involves the *energy equation* which
 65 models the transient heat conduction inside the TPS, and the *pseudo-elasticity equation*,
 66 which models the mesh motion due to surface recession. The governing PDEs for the ablating
 67 TPS are summarized in this section.

68 **Energy Equation** Consider a generic domain $\Omega \subset \mathbb{R}^d$, $d = 2$ or 3 , illustrated in Fig. 1. Let
 69 $\partial\Omega = \Gamma_q \cup \Gamma_T$ and $\Gamma_q \cap \Gamma_T = \emptyset$, where a Neumann $q_b(x, t)$ boundary condition is prescribed
 70 on the Γ_q boundary, and represents the surface exposed to the hypersonic boundary layer.
 71 The Dirichlet $T_b(x, t)$ boundary condition is prescribed on the boundary Γ_T . The TPS is
 72 divided into N non-overlapping components $\{\Omega_i\}_{i=1}^N$, as illustrated in Fig. 1 for $N = 2$.
 73 The i -th component Ω_i is associated with material properties $(\rho_i, c_{p,i}, \mathbf{k}_i)$, that are assumed
 74 to be continuous within one component, and can be discontinuous across two neighboring
 75 components.

76 The transient heat conduction is described by the energy equation,

$$\rho c_p \left(\frac{\partial T}{\partial t} + \tilde{\mathbf{v}}(x, t) \cdot \nabla T \right) - \nabla \cdot (\mathbf{k} \nabla T) = 0, \quad x \in \Omega \quad (1a)$$

$$-\mathbf{k} \nabla T \cdot \mathbf{n} = q_b(x, t), \quad x \in \Gamma_q \quad (1b)$$

$$T(x, t) = T_b(x, t), \quad x \in \Gamma_T \quad (1c)$$

$$T(x, 0) = T_0(x), \quad x \in \Omega \quad (1d)$$

77 where the density ρ is constant, while the heat capacity c_p and thermal conductivity $\mathbf{k} \in \mathbb{R}^{d \times d}$
78 may depend on temperature. In the order they appear, the terms in eq. (1a) include, the
79 unsteady energy storage, heat conduction, temperature advection due to mesh motion, and
80 source terms due to boundary conditions. The boundary conditions for the energy equation
81 includes Neumann eq. (1b) and Dirichlet eq. (1c) on Γ_T .

82 An Abirtrary Lagrangian-Eulerian (ALE) description is used to account for mesh motion
83 due to surface recession, where $\tilde{\mathbf{v}}(x, t)$ is the relative velocity of the material with respect to
84 the mesh,

$$\tilde{\mathbf{v}}(x, t) = \mathbf{v}_s(x, t) - \mathbf{v}_m(x, t) \quad (2)$$

85 where $\mathbf{v}_s(x, t)$ and $\mathbf{v}_m(x, t)$ are the physical material velocity and mesh velocity, respectively.
86 In this work, the physical material velocity is assumed to be zero, i.e., $\mathbf{v}_s(x, t) = \mathbf{0}$, and thus
87 the relative velocity is simply the negative of the mesh velocity, $\tilde{\mathbf{v}}(x, t) = -\mathbf{v}_m(x, t)$.

88 **Pseudo-Elasticity Equation** The mesh motion is described by the steady-state pseudo-
89 elasticity equation without body forces,

$$\nabla \cdot \boldsymbol{\sigma}(\mathbf{w}) = \mathbf{0}, \quad \forall t \in \mathcal{T}, \quad \mathbf{x} \in \Omega \quad (3a)$$

$$\mathbf{w}(\mathbf{x}, t) = \mathbf{w}_q(\mathbf{x}, t), \quad \forall t \in \mathcal{T}, \quad \mathbf{x} \in \Gamma_q \quad (3b)$$

$$\mathbf{w}(\mathbf{x}, t) = \mathbf{0}, \quad \forall t \in \mathcal{T}, \quad \mathbf{x} \notin \Gamma_q \quad (3c)$$

$$\mathbf{w}(\mathbf{x}, 0) = \mathbf{0}, \quad \forall \mathbf{x} \in \Omega \quad (3d)$$

90 where the stress tensor $\boldsymbol{\sigma}$ is related to the strain tensor $\boldsymbol{\epsilon}(\mathbf{w})$ through Hooke's law,

$$\boldsymbol{\sigma}(\mathbf{w}) = \mathbb{D} : \boldsymbol{\epsilon}(\mathbf{w})$$

91 where \mathbb{D} is the fourth-order positive definite elasticity tensor, and “ $:$ ” is the double con-
92 traction of the full-order tensor \mathbb{D} with the second-order tensor $\boldsymbol{\epsilon}$. The elasticity tensor
93 ordinarily possess a number of symmetries, effectively reducing the number of components

94 that describe it [2]. The symmetric strain tensor ϵ measures the deformation of the mesh
 95 due to displacements $\mathbf{w}(x, t)$, and is defined as,

$$\epsilon(\mathbf{w}) = \frac{1}{2} (\nabla \mathbf{w} + \nabla \mathbf{w}^\top)$$

96 The “material” properties for the mesh are chosen to tailor the mesh deformation, and need
 97 not represent the actual material being modeled [1].

98 For the pseudo-elasticity equations, the boundary conditions include prescribed displace-
 99 ments $\mathbf{w}_q(x, t)$ on the heated boundary Γ_q in eq. (3b), and zero displacements on the unheated
 100 boundaries in eq. (3c). The initial condition for the mesh displacements is zero in eq. (3d).
 101 Particularly, the surface velocity due to the ablating material is a function of the surface
 102 temperature $T_q(x, t)$ for $x \in \Gamma_q$ on the heated boundary. For the i -th material component,
 103 the mesh velocity on the heated boundary is imposed based on the following relation,

$$\hat{\mathbf{n}} \cdot \mathbf{v}_m(x, t) = f(T_q(x, t)), \quad x \in \Gamma_q \quad (4)$$

104 where $\hat{\mathbf{n}}$ is the unit normal vector on the heated boundary Γ_q , and f is a function obtained
 105 from tabulated data for the material, commonly referred to as a B' table [1]. The B' table
 106 provides a model for the recession velocity as a function of the surface temperature, and is
 107 pre-computed based on high-fidelity simulations of the ablation process for a one-dimensional
 108 slab of the material, and is independent of the TPS geometry. Provided the surface velocity,
 109 the boundary condition in eq. (5) for the mesh displacements are computed by integrating
 110 the surface velocity over time,

$$\mathbf{w}_q(x, t) = \int_0^t \mathbf{v}_m(x, \tau) d\tau \quad (5)$$

111 2.2 Full-Order Model: Finite-Element Method

112 To obtain the full-order numerical solution, the energy quation is spatially discretized using
 113 variational principles of the Discontinuous Galerkin (DG) method [3], while the pseudo-
 114 elasticity equation is discretized using the standard FEM; the result is a high-dimensional
 115 system of ODEs describing the tempoeral evolution of the temperature field and mesh dis-
 116 placements. Note that the choice of DG approach here is mainly for theoretical convenience
 117 in the coarse-graining formulation, and is exclusively performed on the energy equation as
 118 the *quantities of interest* (QoIs) or *observables* correspond to the surface temperatures. The
 119 equivalence between DG and FEM is noted upon their convergence.

120 Consider a conforming mesh partition domain, where each element belongs to one and

¹²¹ only one component. Denote the collection of all M elements as $\{E_i\}_{i=1}^M$. In an element E_i ,
¹²² its shared boundaries with another element E_j , Neumann BC, and Dirichlet BC are denoted
¹²³ as e_{ij} , e_{iq} , and e_{iT} , respectively. Lastly, $|e|$ denotes the length ($n_d = 2$) or area ($n_d = 3$) of a
¹²⁴ component boundary e .

¹²⁵ For the i -th element, use a set of P trial functions, such as polynomials, to represent the
¹²⁶ temperature distribution,

$$T_i(x, t) = \sum_{l=1}^P \phi_l^i(x) u_l^i(t) \equiv \boldsymbol{\phi}_i^\top(x) \mathbf{u}_i(t), \quad i = 1, 2, \dots, M \quad (6)$$

¹²⁷ Without loss of generality, the trial functions are assumed to be orthogonal, so that,

$$\int_{E_i} \phi_l^i(x) \phi_k^i(x) d\Omega = 0, \quad l \neq k$$

¹²⁸ where δ_{lk} is the Kronecker delta function. Furthermore, for simplicity, choose $\phi_1^i = 1$. Thus,
¹²⁹ by orthogonality,

$$\int_{E_i} \phi_1^i(x) d\Omega = |E_i|, \quad \int_{E_i} \phi_k^i(x) d\Omega = 0, \quad k = 2, 3, \dots, P$$

¹³⁰ Under the choice of basis functions, u_1^i is simply the average temperature of element E_i ,
¹³¹ denoted as \bar{u}_i .

¹³² By standard variational processes, e.g., [3], the element-wise governing equation is de-
¹³³ noted as,

$$\mathbf{A}_i \dot{\mathbf{u}}_i = (\mathbf{B}_i + \mathbf{C}_i) \mathbf{u}_i + \sum_{j \in \mathcal{N}_i \cup \{T_b\}} (\mathbf{B}_{ij}^i \mathbf{u}_i + \mathbf{B}_{ij}^j \mathbf{u}_j) + \mathbf{f}_i(t), \quad \text{for } i = 1, 2, \dots, M \quad (7)$$

¹³⁴ which is collected as the following ODE for the all the elements in the mesh,

$$\mathbf{A}(\mathbf{u}) \dot{\mathbf{u}} = [\mathbf{B}(\mathbf{u}) + \mathbf{C}(\mathbf{u})] \mathbf{u} + \mathbf{f}(t) \quad (8)$$

¹³⁵ where $\mathbf{u} = [\mathbf{u}_1, \mathbf{u}_2, \dots, \mathbf{u}_M]^\top \in \mathbb{R}^{MP}$ includes all the DG variables, $\mathbf{f} \in \mathbb{R}^{MP}$ is the exter-
¹³⁶ nal forcing, and the system matrices \mathbf{A} , \mathbf{B} , and \mathbf{C} are the matrices due to heat capacity,
¹³⁷ heat conduction, and temperature advection due to mesh motion, respectively. A detailed
¹³⁸ derivation of eqs. (7) and (8) and their matrices is provided in Appendix A.

¹³⁹ **2.3 Reduced-Physics Model**

¹⁴⁰ The RPM for predicting the response of the ablating TPS consists of two components: (1)
¹⁴¹ the *lumped-capacitance model* (LCM), and (2) the *surface velocity model* (SVM). The LCM is
¹⁴² described as a first-order system of ODEs for predicting the average temperatures inside the
¹⁴³ components of the TPS, and provides a low-fidelity under-estimation for the component's
¹⁴⁴ surface temperature. The SVM provides a relation between the surface temperature and
¹⁴⁵ the surface recession velocity based on pre-computed B' tables for the material, specifying
¹⁴⁶ the one-dimensional surface displacements through time integration. The LCM and SVM
¹⁴⁷ are combined to define the RPM, providing low-fidelity estimates for the temperatures and
¹⁴⁸ surface recession of the ablating TPS.

¹⁴⁹ **2.3.1 Lumped Capacitance Model**

¹⁵⁰ A general form of the LCM is provided in this section; details regarding the derivation for
¹⁵¹ the four-component TPS in Fig. 2 are provided in Appendix A. The LCM is a classical
¹⁵² physics-based low-order model for predicting the temporal variation of average temperature
¹⁵³ in multiple interconnected components [4]. The LCM is derived at the component level from
¹⁵⁴ a point of view of energy conservation, and leads to the following system of ODEs for the
¹⁵⁵ average temperatures on the components,

$$\bar{\mathbf{A}}\dot{\bar{\mathbf{u}}} = \bar{\mathbf{B}}\bar{\mathbf{u}} + \bar{\mathbf{f}}(t) \quad (9)$$

¹⁵⁶ Where the states and inputs,

$$\bar{\mathbf{u}} = [\bar{u}_1, \bar{u}_2, \dots, \bar{u}_N]^\top \in \mathbb{R}^N, \quad \bar{\mathbf{f}} = [\bar{f}_1, \bar{f}_2, \dots, \bar{f}_N]^\top \in \mathbb{R}^N \quad (10)$$

¹⁵⁷ include the average temperatures $\bar{\mathbf{u}}$ and forcing inputs $\bar{\mathbf{f}}$ for the N components. For $i, j =$
¹⁵⁸ $1, 2, \dots, N$ the (i, j) -th elements of the $\bar{\mathbf{A}} \in \mathbb{R}^{N \times N}$, $\bar{\mathbf{B}} \in \mathbb{R}^{N \times N}$, and $\bar{\mathbf{f}} \in \mathbb{R}^N$ matrices are
¹⁵⁹ given by,

$$\bar{A}_i = \begin{cases} \int_{\Omega_i} \rho c_p d\Omega_i, & i = j \\ 0, & i \neq j \end{cases}, \quad \bar{B}_{ij} = \begin{cases} \sum_{j \in \mathcal{N}_i \cup \{T_b\}} \bar{B}_{ij}^i, & i = j \\ \bar{B}_{ij}^{(j)}, & i \neq j \end{cases}, \quad (11a)$$

$$\mathbf{f}_i = \begin{cases} |e_{iq}| \bar{q}_i + \frac{|e_{iT}|}{R_i} \bar{T}_i, & i = j \\ 0, & i \neq j \end{cases} \quad (11b)$$

160 where,

$$\bar{q}_i = \frac{1}{|e_{iq}|} \int_{e_{iq}} q_b de_{iq}, \quad \bar{T}_i = \frac{1}{|e_{iT}|} \int_{e_{iT}} T_b de_{iT}, \quad \bar{B}_{ij}^i = -\frac{|e_{ij}|}{R_{ij}}, \quad \bar{B}_{ij}^j = \frac{|e_{ij}|}{R_{ij}} \quad (12)$$

161 2.3.2 Surface Velocity Model

162 The displacement is assumed to be *one-dimensional* on the heated boundary Γ_q , i.e., the
163 surface recedes only in the direction of the applied load, and occurs only for $\tilde{N} \leq N$ compon-
164 ents. For example, in Fig. 2, the surface displacement on the heated boundary occurs only
165 in the negative y -direction for the three components exposed to the hypersonic boundary
166 layer; the fourth component is the substrate and does not ablate. For the i -th component,
167 the SVM considered in this work takes the form,

$$\dot{\mathbf{w}} = \boldsymbol{\Xi} \bar{\mathbf{u}} - \tilde{\mathbf{f}} \quad (13)$$

168 where $\boldsymbol{\Xi} = \text{diag}(\xi_1, \dots, \xi_{\tilde{N}})$ and $\tilde{\mathbf{f}} = (\xi_1 \bar{u}_{0,1}, \dots, \xi_{\tilde{N}} \bar{u}_{0,\tilde{N}})^\top$. The constants ξ_i are small
169 material-dependent constants, determined from the B' table, and $\bar{u}_{0,i}$ is the constant initial
170 temperature of the component. The SVM provides a relation between the surface tempera-
171 ture and the surface recession velocity based on pre-computed B' tables for the material.

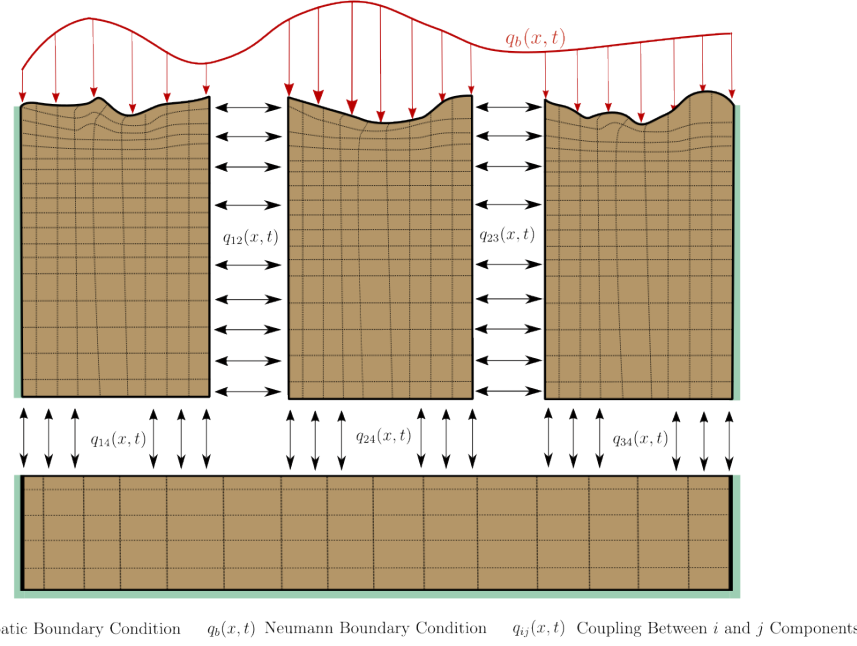
172 2.3.3 Coupled Reduced-Physics Model

173 The LCM and SVM are combined to define the RPM for predicting the thermo-ablative
174 response of the TPS. Specifically, the RPM is defined as the LCM as in eq. (9), where the
175 *geometry-dependent matrices* $\bar{\mathbf{A}}$, $\bar{\mathbf{B}}$, and $\bar{\mathbf{f}}$ are updated at each time step based on the current
176 surface displacements provided by the SVM. Assuming the same material properties for the
177 ablative components, the RPM is written as,

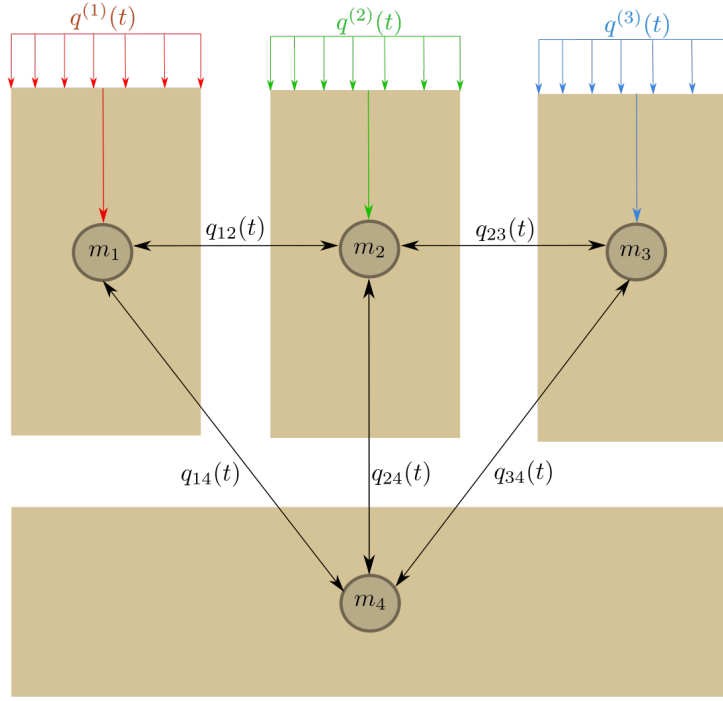
$$\mathcal{A}(\mathbf{s})\dot{\mathbf{s}} = \mathcal{B}(\mathbf{s})\mathbf{s} + \mathcal{F}(t) \quad (14)$$

178 where the state $\mathbf{s} = [\bar{\mathbf{u}}, \mathbf{w}]^\top \in \mathbb{R}^{N+\tilde{N}}$ includes the average temperatures for N components
179 and the surface displacements \tilde{N} ablating components. The matrices are given as,

$$\mathcal{A} = \begin{bmatrix} \bar{\mathbf{A}}(\mathbf{w}) & \mathbf{0} \\ \mathbf{0} & \mathbf{I} \end{bmatrix}, \quad \mathcal{B}(\mathbf{s}) = \begin{bmatrix} \bar{\mathbf{B}}(\mathbf{w}) & \mathbf{0} \\ \boldsymbol{\Xi} & \mathbf{0} \end{bmatrix}, \quad \mathcal{F}(t) = \begin{bmatrix} \bar{\mathbf{f}}(t) \\ -\tilde{\mathbf{f}} \end{bmatrix} \quad (15)$$



(a) TPS Decomposition



(b) Lumped Mass Representation

Figure 2: Partition of the TPS into three ablating and one non-ablating components with the corresponding lumped-mass representation.

180 **2.4 Summary of Modeling Approaches**

181 The FOM (i.e., DG-FEM) and RPM (i.e., LCM) are two different but mathematically con-
182 nected solution strategies. Specifically, the LCM in eq. (9) not only resembles the functional
183 form of the DG model in eq. (8), but can be viewed as a special case of the latter, where the
184 mesh partition is extremely coarse, and the trial and test functions are piece-wise constants.
185 For example, consider the case where each component Ω_i is treated as one single element,
186 and each element employs one constant basis function $\phi_i = 1$. The element-wise DG model
187 in eq. (7) simplifies into a scalar ODE that ignores advection effects due to mesh motion,

$$\mathbf{A}^{(i)} = \bar{A}_i, \quad \mathbf{C}^{(i)} = 0, \quad \mathbf{B}_{ij}^{(i)} = -\sigma|e_{ij}|, \quad \mathbf{B}_{ij}^{(j)} = \sigma|e_{ij}|, \quad \mathbf{f}_i = |e_{iq}|\bar{q}_i + \sigma|e_{iT}|\bar{T}_i \quad (16)$$

188 Clearly, the LCM is a coarse zeroth-order DG model with the inverse of thermal resistance
189 chosen as the element-wise penalty factors. Or conversely, the DG model is a refined version
190 of LCM via *hp*-adaptation.

191 The FOM and RPM represent two extremes in the modeling fidelity and computational
192 cost spectrum. On one hand, the FOM is the most accurate but computationally expensive
193 to evaluate due to the fine mesh discretizations for both the temperature and displacement
194 fields, leading to possibly millions of state variables. On the other hand, the RPM considers
195 only the average temperature of the material as the state variable, considerably reducing
196 the computational cost, but sacrificing local temperature information and thus neglecting
197 higher-order effects due to mesh motion. Thus, neither the FOM nor the RPM is a universal
198 approach for real-world analysis, design, and optimization tasks for ablating TPS, where
199 thousands of high-fidelity model evaluations may be necessary. This issue motivates the
200 development of the PIROM, which can achieve the fidelity of FOM at a computational cost
201 close to the RPM, while maintaining the generalizability to model parameters.

202 **3 Physics-Infused Reduced-Order Modeling**

203 The formulation of PIROM for ablating TPS starts by connecting the FOM, i.e., DG-FEM,
204 and the RPM, i.e., the LCM, via a coarse-graining procedure. This procedure pinpoints
205 the missing dynamics in the LCM when compared to DG-FEM. Subsequently, the Mori-
206 Zwanzig (MZ) formalism is employed to determine the model form for the missing dynamics
207 in PIROM. Lastly, the data-driven identification of the missing dynamics in PIROM is
208 presented.

209 **3.1 Deriving the Reduced-Physics Model via Coarse-Graining**

210 The LCM is derived from a full-order DG on a fine mesh via coarse graining. This pro-
211 cess constraints the trial function space of a full-order DG model to a subset of piece-wise
212 constants, so that the variables \mathbf{u} , matrices \mathbf{A} , \mathbf{B} , and \mathbf{C} , and forcing vector \mathbf{f} are all ap-
213 proximated using a single state associated to the average temperature. The details of the
214 projection are described next.

215 **3.1.1 Coarse-Graining of States**

216 Consider a DG model as in eq. (8) for M elements and an LCM as in eq. (9) for N components;
217 clearly $M \gg N$. Let $\mathcal{V}_j = \{i | E_i \in \Omega_j\}$ be the indices of the elements belonging to the j -th
218 component, so $E_i \in \Omega_j$ for all $i \in \mathcal{V}_j$. The number of elements in the j -th component is $|\mathcal{V}_j|$.
219 The average temperature on Ω_j is,

$$\bar{u}_j = \frac{1}{|\Omega_j|} \sum_{i \in \mathcal{V}_j} \int_{E^{(i)}} \boldsymbol{\phi}^{(i)}(x)^T \mathbf{u}^{(i)} d\Omega = \frac{1}{|\Omega_j|} \sum_{i \in \mathcal{V}_j} |E_i| \boldsymbol{\varphi}_i^{j\top} \mathbf{u}^{(i)}, \quad j = 1, 2, \dots, N \quad (17)$$

220 where $|\Omega_j|$ and $|E_i|$ denote the area ($d = 2$) or volume ($d = 3$) of component j and element
221 i , respectively. The orthogonal basis functions are defined as $\boldsymbol{\varphi}_i^{j\top} = [1, 0, \dots, 0]^\top \in \mathbb{R}^P$.

222 Conversely, given the average temperatures of the N components, $\bar{\mathbf{u}}$, the states of an
223 arbitrary element E_i is written as,

$$\mathbf{u}^{(i)} = \sum_{k=1}^N \boldsymbol{\varphi}_i^k \bar{u}_k + \delta \mathbf{u}^{(i)}, \quad i = 1, 2, \dots, M \quad (18)$$

224 where $\boldsymbol{\varphi}_i^k = 0$ if $i \notin \mathcal{V}_k$, and $\delta \mathbf{u}^{(i)}$ represents the deviation from the average temperature and
225 satisfies the orthogonality condition $\boldsymbol{\varphi}_i^k \boldsymbol{\varphi}_i^{j\top} = 0$ for all k .

226 Equations eqs. (17) and (18) are combined and written in matrix form as,

$$\bar{\mathbf{u}} = \boldsymbol{\Phi}^+ \mathbf{u}, \quad \mathbf{u} = \boldsymbol{\Phi} \mathbf{u} + \delta \mathbf{u} \quad (19)$$

227 where $\boldsymbol{\Phi} \in \mathbb{R}^{MP \times N}$ is a matrix of $M \times N$ blocks, with the (i, j) -th block as $\boldsymbol{\varphi}_i^j$, $\boldsymbol{\Phi}^+ \in \mathbb{R}^{N \times MP}$
228 is the left inverse of $\boldsymbol{\Phi}$, with the (i, j) -th block as $\boldsymbol{\varphi}_i^{j+} = \frac{|E_i|}{|\Omega_j|} \boldsymbol{\varphi}_i^{j\top}$, and $\delta \mathbf{u}$ is the collection of
229 deviations. By their definitions, $\boldsymbol{\Phi}^+ \boldsymbol{\Phi} = \mathbf{I}$ and $\boldsymbol{\Phi}^+ \delta \mathbf{u} = \mathbf{0}$.

²³⁰ **3.1.2 Coarse-Graining of Dynamics**

²³¹ Next, consider a function of states in the form of $\mathbf{M}(\mathbf{u})\mathbf{g}(\mathbf{u})$, where $\mathbf{g} : \mathbb{R}^{MP} \rightarrow \mathbb{R}^{MP}$
²³² is a vector-valued function, and $\mathbf{M} : \mathbb{R}^{MP} \rightarrow \mathbb{R}^{p \times MP}$ is a matrix-valued function with an
²³³ arbitrary dimension p . Define the projection matrix $\mathbf{P} = \Phi\Phi^+$ and the projection operator
²³⁴ \mathcal{P} as,

$$\begin{aligned}\mathcal{P}[\mathbf{M}(\mathbf{u})\mathbf{g}(\mathbf{u})] &= \mathbf{M}(\mathbf{Pu})\mathbf{g}(\mathbf{Pu}) \\ &= \mathbf{M}(\Phi\bar{\mathbf{u}})\mathbf{g}(\Phi\bar{\mathbf{u}})\end{aligned}\quad (20)$$

²³⁵ so that the resulting function depends only on the average temperatures $\bar{\mathbf{u}}$. Correspondingly,
²³⁶ the residual operator $\mathcal{Q} = \mathcal{I} - \mathcal{P}$, and $\mathcal{Q}[\mathbf{M}(\mathbf{u})\mathbf{g}(\mathbf{u})] = \mathbf{M}(\mathbf{u})\mathbf{g}(\mathbf{u}) - \mathbf{M}(\Phi\bar{\mathbf{u}})\mathbf{g}(\Phi\bar{\mathbf{u}})$. When
²³⁷ the function is not separable, the projection operator is simply defined as $\mathcal{P}[\mathbf{g}(\mathbf{u})] = \mathbf{g}(\mathbf{Pu})$.

²³⁸ Subsequently, the operators defined above are applied to coarse-grain the dynamics. First,
²³⁹ write the DG-FEM in eq. (8) as,

$$\dot{\mathbf{u}} = \mathbf{A}(\mathbf{u})^{-1}\mathbf{B}(\mathbf{u})\mathbf{u} + \mathbf{A}(\mathbf{u})^{-1}\mathbf{C}(\mathbf{u})\mathbf{u} + \mathbf{A}(\mathbf{u})^{-1}\mathbf{f}(t) \quad (21)$$

²⁴⁰ and multiply both sides by Φ^+ to obtain,

$$\Phi^+\dot{\mathbf{u}} = \Phi^+(\Phi\bar{\mathbf{u}} + \delta\dot{\mathbf{u}}) = \dot{\bar{\mathbf{u}}} = \Phi^+\mathbf{r}(\mathbf{u}, t) \quad (22)$$

²⁴¹ Apply the projection operator \mathcal{P} and the residual operator \mathcal{Q} to the right-hand side to obtain,

$$\dot{\bar{\mathbf{u}}} = \mathcal{P}[\Phi^+\mathbf{r}(\mathbf{u}, t)] + \mathcal{Q}[\Phi^+\mathbf{r}(\mathbf{u}, t)] \equiv \mathbf{r}^{(1)}(\mathbf{u}, t) + \mathbf{r}^{(2)}(\mathbf{u}, t) \quad (23)$$

²⁴² where $\mathbf{r}^{(1)}(\mathbf{u}, t)$ is resolved dynamics that depends on $\bar{\mathbf{u}}$ only, and $\mathbf{r}^{(2)}(\mathbf{u}, t)$ is the un-resolved
²⁴³ or residual dynamics. Detailed derivations and analysis of $\mathbf{r}^{(1)}(\mathbf{u}, t)$ and $\mathbf{r}^{(2)}(\mathbf{u}, t)$ can be
²⁴⁴ found in the Appendix.

²⁴⁵ It follows from Ref. [x] that the resolved dynamics is exactly the LCM, where the advection
²⁴⁶ term reduces to zero, i.e., $\bar{\mathbf{C}}(\bar{\mathbf{u}}) = \mathbf{0}$ as shown in the Appendix. Using the notation from
²⁴⁷ eq. (9), it follows that,

$$\begin{aligned}\mathbf{r}^{(1)}(\mathbf{u}, t) &= \bar{\mathbf{A}}(\bar{\mathbf{u}})^{-1}\bar{\mathbf{B}}(\bar{\mathbf{u}})\bar{\mathbf{u}} + \bar{\mathbf{A}}(\bar{\mathbf{u}})^{-1}\bar{\mathbf{C}}(\bar{\mathbf{u}})\bar{\mathbf{u}} + \bar{\mathbf{A}}(\bar{\mathbf{u}})^{-1}\bar{\mathbf{f}}(\bar{\mathbf{u}}) \\ &= \bar{\mathbf{A}}(\bar{\mathbf{u}})^{-1}\bar{\mathbf{B}}(\bar{\mathbf{u}})\bar{\mathbf{u}} + \bar{\mathbf{A}}(\bar{\mathbf{u}})^{-1}\bar{\mathbf{f}}(t)\end{aligned}\quad (24)$$

248 where the following relations hold,

$$\bar{\mathbf{A}}(\bar{\mathbf{u}}) = \mathbf{W} (\Phi^+ \mathbf{A} (\Phi \bar{\mathbf{u}})^{-1} \Phi)^{-1} \quad \bar{\mathbf{C}}(\bar{\mathbf{u}}) = \mathbf{0} \quad (25a)$$

$$\bar{\mathbf{B}}(\bar{\mathbf{u}}) = \mathbf{W} \Phi^+ \mathbf{B} (\Phi \bar{\mathbf{u}}) \Phi \quad \bar{\mathbf{f}}(t) = \mathbf{W} \Phi^+ \mathbf{f} \quad (25b)$$

249 where $\mathbf{W} \in \mathbb{R}^{N \times N}$ is a diagonal matrix with the i -th element as $[\mathbf{W}]_{ii} = |\mathcal{V}_k|$ if $i \in$
250 \mathcal{V}_k . As shown in the Appendix, the examination of the second residual term $\mathbf{r}^{(2)}(\mathbf{u}, t)$ in
251 eq. (23) reveals the physical sources of missing dynamics in the LCM: the approximation of
252 non-uniform temperature within each component as a constant, and the elimination of the
253 advection term due to coarse-graining.

254 In sum, the above results not only show that the LCM is a result of coarse-graining of
255 the full-order DG-FEM, but also reveal the discrepancies between the LCM and the DG-
256 FEM. In the subsequent section, the discrepancies will be corrected to produce the proposed
257 PIROM.

258 3.2 Formulation of Reduced-Order Model

259 The Mori-Zwanzig (MZ) formalism is an operator-projection technique used to derive ROMs
260 for high-dimensional dynamical systems, especially in statistical mechanics and fluid dynam-
261 ics Parish,Duraisamy . It provides an exact reformulation of the full-order dynamics in terms
262 of a subset of resolved variables. The proposed ROM is subsequently developed based on
263 such reformulation. Equation eq. (23) shows that the DG-FEM dynamics can be decomposed
264 into the resolved dynamics $\mathbf{r}^{(1)}(\mathbf{u}, t)$ and the orthogonal dynamics $\mathbf{r}^{(2)}(\mathbf{u}, t)$, in the sense of
265 $\mathcal{P}\mathbf{r}^{(2)} = 0$. In this case, the MZ formalism can be invoked to express the dynamics $\bar{\mathbf{u}}$ in terms
266 of $\bar{\mathbf{u}}$ alone as the projected Generalized Langevin Equation (GLE) Parish,Duraisamy ,

$$\dot{\bar{\mathbf{u}}}(t) = \mathbf{r}^{(1)}(\bar{\mathbf{u}}, t) + \int_0^t \tilde{\boldsymbol{\kappa}}(t, s, \bar{\mathbf{u}}) ds \quad (26)$$

267 where the first term is Markovian, and the integral term is referred to as the memory. The
268 integral term is non-Markovian, accounting for impact of past resolved states on the current
269 states through their interactions with the un-resolved states.

270 Next, to further inform the subsequent derivation of the ROM, the kernel $\tilde{\mathbf{k}}$ is examined
271 via a leading-order expansion, based on prior work x; this can be viewed as an analog of
272 zeroth-order holding in linear system theory with a sufficiently small time step. In this case,
273 the memory kernel is approximated as,

$$\tilde{\boldsymbol{\kappa}}(t, s, \bar{\mathbf{u}}) \approx \mathbf{r}^{(1)}(\bar{\mathbf{u}}, t) \cdot \nabla_{\bar{\mathbf{u}}} \mathbf{r}^{(2)}(\Phi \bar{\mathbf{u}}, t) \quad (27)$$

²⁷⁴ Note that the terms in $\mathbf{r}^{(1)}$ have a common factor $\bar{\mathbf{A}}^{-1}$; this motivates the following heuristic
²⁷⁵ modification of the model form in eq. (26),

$$\dot{\bar{\mathbf{u}}} = \mathbf{r}^{(1)}(\bar{\mathbf{u}}, t) + \bar{\mathbf{A}}^{-1}(\bar{\mathbf{u}}) \int_0^t \boldsymbol{\kappa}(t, s, \bar{\mathbf{u}}) ds \quad (28a)$$

$$\bar{\mathbf{A}}(\bar{\mathbf{u}})\dot{\bar{\mathbf{u}}} = \bar{\mathbf{B}}(\bar{\mathbf{u}})\bar{\mathbf{u}} + \bar{\mathbf{f}}(t) + \int_0^t \boldsymbol{\kappa}(t, s, \bar{\mathbf{u}}) ds \quad (28b)$$

²⁷⁶ where the original kernel $\tilde{\boldsymbol{\kappa}}$ is effectively normalized by $\bar{\mathbf{A}}^{-1}$. Intuitively, such choice of kernel
²⁷⁷ reduces its dependency on the averaged material properties, and simplifies the subsequent
²⁷⁸ design of model form.

²⁷⁹ Subsequently, the hidden states are introduced to “Markovianize” the system eq. (26).
²⁸⁰ In this manner, eq. (28b) is converted into a pure state-space model, with the functional
²⁸¹ form of the LCM retained; since LCM is a physics-based model, then it encodes the phys-
²⁸² ical information and retains explicit parametric dependence of the problem. Consider the
²⁸³ representation of the kernel as a finite sum of simpler functions, e.g., exponentials,

$$\boldsymbol{\kappa}(t, s, \bar{\mathbf{u}}) = \sum_{j=1}^m \mathcal{K}_j(t, s, \bar{\mathbf{u}}) [\mathbf{p}_j + \mathbf{d}_j(\bar{\mathbf{u}})] \phi_j(s, \bar{\mathbf{u}}) \quad (29)$$

²⁸⁴ where,

$$\mathcal{K}_j(t, s, \bar{\mathbf{u}}) = e^{-\int_s^t (\lambda_j + e_j(\bar{\mathbf{u}})) d\tau}, \quad \phi_j(s, \bar{\mathbf{u}}) = \mathbf{q}_j^\top \bar{\mathbf{u}}(s) + \mathbf{g}_j(\bar{\mathbf{u}})^\top \bar{\mathbf{u}}(s) + \mathbf{r}_j^\top \bar{\mathbf{f}}(s) \quad (30)$$

²⁸⁵ with suitable coefficients $\mathbf{p}_j, \mathbf{d}_j, \mathbf{q}_j, \mathbf{g}_j, \mathbf{r}_j \in \mathbb{R}^N$ and decay rates $\lambda_j, e_j(\bar{\mathbf{u}}) > 0$, that need to
²⁸⁶ be identified from data.

²⁸⁷ Define the hidden states as,

$$\beta_j(t) = \int_0^t \mathcal{K}_j(s, \bar{\mathbf{u}}) \phi_j(s, \bar{\mathbf{u}}) ds \quad (31)$$

²⁸⁸ then through its differentiation with respect to time,

$$\dot{\beta}_j(t) = -[\lambda_j + e_j(\bar{\mathbf{u}})] \beta_j(t) + \mathbf{q}_j^\top \bar{\mathbf{u}}(t) + \mathbf{g}_j(\bar{\mathbf{u}})^\top \bar{\mathbf{u}}(t) + \mathbf{r}_j^\top \bar{\mathbf{f}}(t) \quad (32)$$

²⁸⁹ and the memory term becomes,

$$\int_0^t \boldsymbol{\kappa}(t, s, \bar{\mathbf{u}}) ds = \sum_{j=1}^m [\mathbf{p}_j + \mathbf{d}_j(\bar{\mathbf{u}})] \beta_j(t) \quad (33)$$

290 Then, eq. (28b) is recast as the extended Markovian system,

$$\bar{\mathbf{A}}(\bar{\mathbf{u}})\dot{\bar{\mathbf{u}}} = \bar{\mathbf{B}}(\bar{\mathbf{u}})\bar{\mathbf{u}} + [\mathbf{P} + \mathbf{D}(\bar{\mathbf{u}})]\boldsymbol{\beta} + \bar{\mathbf{f}}(t) \quad (34a)$$

$$\boldsymbol{\beta} = [-\boldsymbol{\Lambda} + \mathbf{E}(\bar{\mathbf{u}})]\boldsymbol{\beta} + [\mathbf{Q} + \mathbf{G}(\bar{\mathbf{u}})]\bar{\mathbf{u}} + \mathbf{R}\bar{\mathbf{f}}(t) \quad (34b)$$

291 where,

$$\boldsymbol{\Lambda} = \text{diag}(\lambda_1, \lambda_2, \dots, \lambda_m) \in \mathbb{R}^{m \times m}, \quad \mathbf{P} = [\mathbf{p}_1, \mathbf{p}_2, \dots, \mathbf{p}_m] \in \mathbb{R}^{N \times m} \quad (35a)$$

$$\mathbf{D}(\bar{\mathbf{u}}) = [\mathbf{d}_1(\bar{\mathbf{u}}), \mathbf{d}_2(\bar{\mathbf{u}}), \dots, \mathbf{d}_m(\bar{\mathbf{u}})] \in \mathbb{R}^{N \times m}, \quad \mathbf{Q} = [\mathbf{q}_1, \mathbf{q}_2, \dots, \mathbf{q}_m] \in \mathbb{R}^{m \times N} \quad (35b)$$

$$\mathbf{G}(\bar{\mathbf{u}}) = [\mathbf{g}_1(\bar{\mathbf{u}}), \mathbf{g}_2(\bar{\mathbf{u}}), \dots, \mathbf{g}_m(\bar{\mathbf{u}})] \in \mathbb{R}^{m \times N}, \quad \mathbf{R} = [\mathbf{r}_1, \mathbf{r}_2, \dots, \mathbf{r}_m] \in \mathbb{R}^{m \times N} \quad (35c)$$

$$\mathbf{E}(\bar{\mathbf{u}}) = \text{diag}(e_1(\bar{\mathbf{u}}), e_2(\bar{\mathbf{u}}), \dots, e_m(\bar{\mathbf{u}})) \in \mathbb{R}^{m \times m} \quad (35d)$$

292 Since the hidden states $\boldsymbol{\beta}$ serve as the memory, their initial conditions are set to zero, i.e.,
293 $\boldsymbol{\beta}(t_0) = \mathbf{0}$, no memory at the beginning. The physics-infused model in eq. (34) retains the
294 structure of the LCM, while the hidden states account for missing physics through corrections
295 to the stiffness and advection matrices, as well as the forcing term.

296 Lastly, denote the collection of resolved and hidden states as $\mathbf{y} = [\bar{\mathbf{u}}, \boldsymbol{\beta}]^T \in \mathbb{R}^{n_y}$ with
297 $n_y = N + m$, then the proposed PIROM is summarized as,

$$\tilde{\mathbf{A}}\dot{\mathbf{y}} = [\tilde{\mathbf{B}} + \tilde{\mathbf{C}}]\mathbf{y} + \mathbf{H}\bar{\mathbf{f}}(t) \quad (36a)$$

$$\mathbf{z} = \mathbf{M}\mathbf{y} \quad (36b)$$

298 where,

$$\tilde{\mathbf{A}} = \begin{bmatrix} \bar{\mathbf{A}}(\bar{\mathbf{u}}) & \mathbf{O} \\ \mathbf{O} & \mathbf{I} \end{bmatrix} \in \mathbb{R}^{n_y \times n_y}, \quad \tilde{\mathbf{B}} = \begin{bmatrix} \bar{\mathbf{B}}(\bar{\mathbf{u}}) & \mathbf{P} \\ \mathbf{Q} & -\boldsymbol{\Lambda} \end{bmatrix} \in \mathbb{R}^{n_y \times n_y}, \quad \tilde{\mathbf{C}} = \begin{bmatrix} \mathbf{0} & \mathbf{D}(\bar{\mathbf{u}}) \\ \mathbf{G}(\bar{\mathbf{u}}) & \mathbf{E}(\bar{\mathbf{u}}) \end{bmatrix} \in \mathbb{R}^{n_y \times n_y}, \quad (37a)$$

$$\mathbf{H} = \begin{bmatrix} \mathbf{I} \\ \mathbf{R} \end{bmatrix} \in \mathbb{R}^{n_y \times N}, \quad \mathbf{M} \in \mathbb{R}^{n_z \times n_y} \quad (37b)$$

299 In eq. (36), the terms $\bar{\mathbf{A}}$, $\bar{\mathbf{B}}$, and $\bar{\mathbf{f}}$ are the LCM terms. The collection of matrices,

$$\boldsymbol{\Theta} = \{\mathbf{P}, \mathbf{D}(\bar{\mathbf{u}}), \mathbf{G}(\bar{\mathbf{u}}), \boldsymbol{\Lambda}, \mathbf{E}(\bar{\mathbf{u}}), \mathbf{Q}, \mathbf{G}(\bar{\mathbf{u}}), \mathbf{R}, \mathbf{M}\}, \in \mathbb{R}^{n_\theta} \quad (38)$$

300 are learnable parameters to capture the memory effects. Particularly, the matrices $\mathbf{P}, \boldsymbol{\Lambda}, \mathbf{Q}, \mathbf{R}$
301 are constants that need to be identified from data, and account for the effects of coarse-
302 graining on the stiffness and forcing matrices. The matrices $\mathbf{D}(\bar{\mathbf{u}}), \mathbf{E}(\bar{\mathbf{u}}), \mathbf{G}(\bar{\mathbf{u}})$ are state-

303 dependent matrices, and account for the effects of coarse-graining on the advection matrix.
304 Leveraging the DG-FEM formula for the advection matrix in eq. (47c) in the Appendix, and
305 noting that the mesh displacements are functions of the ablating velocity as in eq. (4), the
306 state-dependent matrices for the i -th component are written as,

$$\mathbf{D}^{(i)}(\bar{\mathbf{u}}) \approx f^{(i)}(\bar{u}^{(i)})\mathbf{D}^{(i)}, \quad \mathbf{E}^{(i)}(\bar{\mathbf{u}}) \approx f^{(i)}(\bar{u}^{(i)})\mathbf{E}^{(i)}, \quad \mathbf{G}^{(i)}(\bar{\mathbf{u}}) \approx f^{(i)}(\bar{u}^{(i)})\mathbf{G}^{(i)} \quad (39)$$

307 where $f^{(i)}(\bar{u}^{(i)})$ is the surface recession velocity function in ?? for the i -th component,
308 and $\mathbf{D}^{(i)}, \mathbf{E}^{(i)}, \mathbf{G}^{(i)}$ are constant matrices to be identified from data. In eq. (36), \mathbf{M} is a
309 fully-populated matrix that extracts the observables, i.e., the surface temperatures, from
310 the PIROM states \mathbf{y} . The PIROM incorporates explicit information on the temperature-
311 dependent material properties through the LCM matrices, as well as the surface recession
312 velocity function through eq. (39). The next step is focused on identifying the unknown
313 parameters Θ characterizing the hidden dynamics.

314 3.3 Learning the Hidden Dynamics from Data

315 The learning of the PIROM is achieved through a neural-ODE like approach [Chen2018](#).
316 For ease of presentation, consider the following compact form of the PIROM in eq. (36),

$$\mathcal{F}(\dot{\mathbf{y}}, \mathbf{y}; \boldsymbol{\xi}, \Theta) = \mathbf{0} \quad (40)$$

317 where $\boldsymbol{\xi}$ defines the parametrization of the problem, i.e., operating conditions, such as the
318 BC's, as well as the material properties. Consider a dataset of N_s high-fidelity trajectories
319 of observables over a time interval $[t_0, t_f]$,

$$\mathcal{D} = \left\{ \left(t_k, \mathbf{z}_{\text{HF}}^{(l)}(t_k), \boldsymbol{\xi}^{(l)} \right) \right\}_{l=1}^{N_s}, \quad k = 0, 1, \dots, K \quad (41)$$

320 The learning problem is formulated as the following differentially-constrained problem,

$$\min_{\Theta} \quad \frac{1}{N_s} \sum_{l=1}^{N_s} \frac{1}{K} \sum_{k=0}^K \left\| \mathbf{z}_{\text{HF}}^{(l)}(t_k) - \mathbf{M}\mathbf{y}^{(l)}(t_k) \right\|_2^2 \quad (42a)$$

$$\text{s.t.} \quad \mathcal{F} \left(\dot{\mathbf{y}}^{(l)}, \mathbf{y}^{(l)}; \boldsymbol{\xi}^{(l)}, \Theta \right) = \mathbf{0}, \quad t \in [t_0, t_f], \quad l = 1, 2, \dots, N_s \quad (42b)$$

$$\mathbf{y}^{(l)}(t_0) = \mathbf{y}_0(\boldsymbol{\xi}^{(l)}), \quad l = 1, 2, \dots, N_s \quad (42c)$$

321 **A Technical Details**

322 This appendix presents the technical details of the PIROM framework applied to the TPS
323 ablation problem. The first section provides the mathematical details for the definition of
324 the DG-FEM. The second section follows the projection procedures from Ref. x, and demon-
325 strates the effects of coarse-graining on the advection matrix. The third section presents the
326 derivation of the LCM model from an energy-conservation perspective.

327 **A.1 Full-Order Model**

328 To obtain the full-order numerical solution, the governing equation is spatially discretized
329 using variational principles of Discontinuous Galerkin (DG) to result in a high-dimensional
330 system of ordinary differential equations (ODEs). The DG-FEM model is written in an
331 element-wise form, which is beneficial for subsequent derivations of the lower-order models.
332 Note that the choice of DG approach here is mainly for theoretical convenience in the sub-
333 sequent coarse-graining formulation. In the numerical results, the full-order TPS ablation
334 simulations is computed using standard FEM instead, and the equivalence between DG and
335 standard FEM is noted upon their convergence.

336 **A.1.1 Domain Discretization**

337 Consider a conforming mesh partition of the domain, as shown in Fig. DOMAIN, where each
338 element belongs to one and only one component. Denote the collection of all M elements
339 as $\{E_i\}_{i=1}^M$. To ease the description of the DG model, a graph structure is employed. The
340 elements are treated as vertices, the set of which is denoted $\mathcal{V} = \{m\}_{m=1}^M$. Two neighboring
341 elements, E_i and E_j , are connected by an edge (i, j) , and the shared boundary between them
342 is denoted e_{ij} . The collection of all edges are denoted \mathcal{E} , and \mathcal{G} is referred to as a graph.
343 In the graph, the edges are unidirected, meaning if $(i, j) \in \mathcal{E}$ then $(j, i) \in \mathcal{E}$. Furthermore,
344 denote the neighbors of the i -th element as $\mathcal{N}_i = \{j | (i, j) \in \mathcal{E}\}$. Lastly, for the ease of
345 notation, introduce two special indices: T for the boundary of an element that overlaps with
346 the Dirichlet boundary condition, and similarly q for the Neumann boundary condition.

³⁴⁷ **A.1.2 Weak Form of Discontinuous Galerkin Method**

³⁴⁸ Choosing appropriate basis functions ϕ_k and ϕ_l and using the Interior Penalty Galerkin
³⁴⁹ (IPG) scheme [3], the variational bilinear form for eq. (1a) is,

$$\sum_{i=1}^M a_{\epsilon,i}(\phi_k, \phi_l) = \sum_{i=1}^M L_i(\phi_k) \quad (43)$$

³⁵⁰ where ϵ is an user-specified parameter and,

$$a_{\epsilon,i}(\phi_k, \phi_l) = \int_{E^{(i)}} \left(\rho c_p \phi_k \frac{\partial \phi_l}{\partial t} + \nabla \phi_k \cdot (\mathbf{k} \nabla \phi_l) - \rho c_p \phi_k \mathbf{v} \cdot \nabla \phi_l \right) dE^{(i)} \quad (44a)$$

$$\begin{aligned} &= - \sum_{j \in \mathcal{N}_i \cup \{T_b\}} \int_{e_{ij}} \{ \mathbf{k} \nabla \phi_k \cdot n \} [\phi_l] de_{ij} + \epsilon \sum_{j \in \mathcal{N}_i \cup \{T_b\}} \int_{e_{ij}} \{ \mathbf{k} \nabla \phi_l \cdot n \} [\phi_k] de_{ij} \\ &\quad + \sigma \sum_{j \in \mathcal{N}_i \cup \{T_b\}} \int_{e_{ij}} [\phi_k] [\phi_l] de_{ij} \end{aligned} \quad (44b)$$

$$L_i(v) = \epsilon \sum_{j \in \mathcal{N}_i \cup \{T_b\}} \int_{e_{ij}} (\mathbf{k} \nabla \phi_l \cdot n) T_b de_{ij} + \int_{e_{iq}} \phi_k q_b de_{iq} + \sigma \int_{e_{iT}} \phi_k T_b de_{iT} \quad (44c)$$

³⁵¹ In the bi-linear form above, the notations $[]$ and $\{ \}$ are respectively the jumps and averages
³⁵² at the boundary e_{ij} share by two elements E_i and E_j ,

$$[u] = u|_{E_i} - u|_{E_j}, \quad \{u\} = \frac{1}{2} \left(u|_{E_i} + u|_{E_j} \right), \quad \text{for } x \in e_{ij} = E_i \cap E_j$$

³⁵³ Furthermore, in the bi-linear form, the terms associated with σ are introduced to enforce
³⁵⁴ the Dirichlet boundary conditions; σ is a penalty factor whose value can depend on the size
³⁵⁵ of an element. Depending on the choice of ϵ , the bi-linear form corresponds to symmetric
³⁵⁶ IPG ($\epsilon = -1$), non-symmetric IPG ($\epsilon = 1$), and incomplete IPG ($\epsilon = 0$). All these schemes
³⁵⁷ are consistent with the original PDE and have similar convergence rate with respect to mesh
³⁵⁸ size. In the following derivations, the case $\epsilon = 0$ is chosen for the sake of simplicity.

³⁵⁹ **A.1.3 Discontinuous Galerkin Model**

³⁶⁰ Next, the DG-based model is written in an element-wise form. For the i -th element, use a
³⁶¹ set of P trial functions to represent the temperature as in eq. (6). Without loss of generality,
³⁶² the trial functions are assumed to be orthogonal, so that $\int_{E^{(i)}} \phi_k^{(i)}(x) \phi_l^{(i)}(x) dx = |E^{(i)}| \delta_{kl}$,
³⁶³ where $|E^{(i)}|$ is the area ($n_d = 2$) or volume ($n_d = 3$) of the i -th element, and δ_{kl} is the
³⁶⁴ Kronecker delta.

³⁶⁵ Using test functions same as trial functions, the dynamics $\mathbf{u}^{(i)}$ is obtained by evaluating

³⁶⁶ the element-wise bi-linear forms,

$$a_{\epsilon,i}(\phi_k^{(i)}, T^{(i)}) = L_i(\phi_k^{(i)}), \quad k = 1, 2, \dots, P \quad (45)$$

³⁶⁷ The above procedure yields,

$$\mathbf{A}^{(i)} \dot{\mathbf{u}}^{(i)} = (\mathbf{B}^{(i)} + \mathbf{C}^{(i)}(t)) \mathbf{u}^{(i)} + \sum_{j \in \mathcal{N}_i \cup \{T_b\}} \left(\mathbf{B}_{ij}^{(i)} \mathbf{u}^{(i)} + \mathbf{B}_{ij}^{(j)} \mathbf{u}^{(j)} \right) + \mathbf{f}^{(i)}(t) \quad (46)$$

³⁶⁸ where for $k, l = 1, 2, \dots, P$,

$$[\mathbf{A}^{(i)}]_{kl} = \int_{E^{(i)}} \rho c_p \phi_k^{(i)} \phi_l^{(i)} dE^{(i)} \quad (47a)$$

$$[\mathbf{B}^{(i)}]_{kl} = - \int_{E^{(i)}} (\nabla \phi_k^{(i)}) \cdot (\mathbf{k} \nabla \phi_l^{(i)}) dE^{(i)} \quad (47b)$$

$$[\mathbf{C}^{(i)}]_{kl} = \int_{E^{(i)}} \rho c_p \phi_k^{(i)} \mathbf{v}^{(i)} \cdot \nabla \phi_l^{(i)} dE^{(i)} \quad (47c)$$

$$[\mathbf{B}_{ij}^{(i)}] = \int_{e_{ij}} \left\{ \mathbf{k} \nabla \phi_k^{(i)} \cdot \hat{n} \right\} \phi_l^{(i)} - \sigma [\phi_k^{(i)}] \phi_l^{(i)} de_{ij} \quad (47d)$$

$$[\mathbf{B}_{ij}^{(j)}] = \int_{e_{ij}} - \left\{ \mathbf{k} \nabla \phi_k^{(i)} \cdot \hat{n} \right\} \phi_l^{(j)} + \sigma [\phi_k^{(i)}] \phi_l^{(j)} de_{ij} \quad (47e)$$

$$[\mathbf{f}^{(i)}]_k = \int_{e_{iq}} \phi_k^{(i)} q_b de_{iq} + \sigma \int_{e_{iT}} \phi_k^{(i)} de_{iT} \quad (47f)$$

³⁶⁹ The matrices $\mathbf{A}^{(i)} \in \mathbb{R}^{P \times P}$, $\mathbf{B}^{(i)} \in \mathbb{R}^{P \times P}$, and $\mathbf{C}^{(i)} \in \mathbb{R}^{P \times P}$ are respectively the capacitance,
³⁷⁰ conductivity, and advection matrices for element i . These matrices depend on ρ , c_p , \mathbf{k} , and
³⁷¹ \mathbf{v} , and hence can be non-linear functions of $\mathbf{u}^{(i)}$. Since the trial functions are orthogonal, if
³⁷² ρc_p is constant within an element, $\mathbf{A}^{(i)}$ is diagonal; otherwise, \mathbf{A}_i is symmetric and positive
³⁷³ definite as $\rho c_p > 0$.

³⁷⁴ For compactness, the element-wise model in eq. (46) is also written in matrix form,

$$\mathbf{A}(\dot{\mathbf{u}}) = [\mathbf{B}(\mathbf{u}) + \mathbf{C}(\mathbf{u})] \mathbf{u} + \mathbf{f}(t) \quad (48)$$

³⁷⁵ where $\mathbf{u} = [\mathbf{u}^{(1)}, \mathbf{u}^{(2)}, \dots, \mathbf{u}^{(M)}]^T \in \mathbb{R}^{MP}$ includes all DG variables, $\mathbf{f} = [\mathbf{f}^{(1)}, \mathbf{f}^{(2)}, \dots, \mathbf{f}^{(M)}]^T \in \mathbb{R}^{MP}$, \mathbf{A} and \mathbf{C} are matrices of M diagonal blocks whose i -th blocks are $\mathbf{A}^{(i)}$ and $\mathbf{C}^{(i)}$, and
³⁷⁶ \mathbf{B} is a matrix of $M \times M$ blocks whose (i, j) -th block is,
³⁷⁷

$$\mathbf{B}_{ij} = \begin{cases} \mathbf{B}^{(i)} + \sum_{j \in \mathcal{N}_i \cup \{T_b\}} \mathbf{B}_{ij}^{(i)}, & i = j \\ \mathbf{B}_{ij}^{(j)}, & i \neq j \end{cases} \quad (49)$$

³⁷⁸ The dependency of \mathbf{A} , \mathbf{B} , and \mathbf{C} on \mathbf{u} is explicitly noted in eq. (48), which is the source of
³⁷⁹ non-linearity in the current TPS problem. Moreover, the mesh velocity \mathbf{v} varies with space
³⁸⁰ and time, and thus the advection matrix \mathbf{C} varies with time as a function of q_b .

³⁸¹ A.2 Coarse-Graining of Dynamics

³⁸² The LCM is obtained by coarse-graining the full-order DG-FEM. This coarse-graining proce-
³⁸³ dure produces resolved $\mathbf{r}^{(1)}(\mathbf{u}, t)$ and residual $\mathbf{r}^{(2)}(\mathbf{u}, t)$ dynamics as in eq. (23). This section
³⁸⁴ presents the detail derivations and magnitude analysis for the resolved and residual dynam-
³⁸⁵ ics.

³⁸⁶ A.2.1 Resolved Dynamics

³⁸⁷ Using eq. (20), the resolved dynamics is computed as follows,

$$\mathbf{r}^{(1)}(\mathbf{u}, t) = \mathcal{P} [\Phi^+ \mathbf{A}(\mathbf{u})^{-1} (\mathbf{B}(\mathbf{u})\mathbf{u} + \mathbf{C}(\mathbf{u})\mathbf{u} + \mathbf{f}(t))] \quad (50a)$$

$$\begin{aligned} &= \Phi^+ \mathbf{A}(\mathbf{Pu})^{-1} \mathbf{PB}(\mathbf{Pu}) \mathbf{Pu} + \Phi^+ \mathbf{A}(\mathbf{Pu})^{-1} \mathbf{PC}(\mathbf{Pu}) \mathbf{Pu} \\ &\quad + \Phi^+ \mathbf{A}(\mathbf{Pu})^{-1} \mathbf{Pf}(t, \mathbf{Pu}) \end{aligned} \quad (50b)$$

$$\begin{aligned} &= \underbrace{\Phi^+ \mathbf{A}(\Phi \bar{\mathbf{u}})^{-1} \Phi}_{\#1} \underbrace{\Phi^+ \mathbf{B}(\Phi \bar{\mathbf{u}}) \Phi \bar{\mathbf{u}}}_{\#2} + \Phi^+ \mathbf{A}(\Phi \bar{\mathbf{u}})^{-1} \Phi \underbrace{\Phi^+ \mathbf{C}(\Phi \bar{\mathbf{u}}) \Phi \bar{\mathbf{u}}}_{\#3} \\ &\quad + \Phi^+ \mathbf{A}(\Phi \bar{\mathbf{u}})^{-1} \Phi \underbrace{\Phi^+ \mathbf{f}(t, \Phi \bar{\mathbf{u}})}_{\#4} \end{aligned} \quad (50c)$$

³⁸⁸ Detailed derivations for the #1, #2, and #4 terms can be found in Ref. [x](#). The effects of
³⁸⁹ coarse-graining on the advection term #3 are analyzed next.

³⁹⁰ **Term #3** The $\mathbf{C}(\mathbf{u}) \in \mathbb{R}^{MP \times MP}$ matrix contains M diagonal of size $P \times P$, since the
³⁹¹ basis functions are defined locally on each element. Therefore, $[\mathbf{C}(\mathbf{u})]_{ij} = \mathbf{0}$ for all $i \neq j$ with
³⁹² $i, j = 1, 2, \dots, M$. It follows that for $k, l = 1, 2, \dots, N$,

$$[\Phi^+ \mathbf{C}(t, \Phi \bar{\mathbf{u}}) \Phi]_{kl} = \sum_{i=1}^M \sum_{j=1}^M \boldsymbol{\varphi}_i^{k+} [\mathbf{C}(t, \Phi \bar{\mathbf{u}})]_{ij} \boldsymbol{\varphi}_j^l \quad (51a)$$

$$= \sum_{i=1}^M \boldsymbol{\varphi}_i^{k+} [\mathbf{C}(t, \Phi \bar{\mathbf{u}})]_{ii} \boldsymbol{\varphi}_i^l \quad (51b)$$

$$= \sum_{i \in \mathcal{V}_k} \boldsymbol{\varphi}_i^{k+} [\mathbf{C}(t, \Phi \bar{\mathbf{u}})]_{ii} \boldsymbol{\varphi}_i^l \quad (51c)$$

393 where in the second row, the fact that $[\mathbf{C}(\mathbf{u})]_{ij} = 0$ for all $i \neq j$ is used, and in the last row,
 394 the fact that $\varphi_i^{k+} = 0$ for all $i \notin \mathcal{V}_k$ is used. Now, considering that $[\mathbf{C}(\mathbf{u})]_{ii}$ has a $(1, 1)$ -th
 395 zero element, i.e., $[C_{11}(t, \Phi\bar{\mathbf{u}})]_{ii} = 0$, and that if $k \neq l$ then $i \notin \mathcal{V}_l$ and thus $\varphi_i^l = \mathbf{0}$, it follows
 396 that for some index $i \in \mathcal{V}_k$,

$$\varphi_i^{k+} [\mathbf{C}(t, \Phi\bar{\mathbf{u}})]_{ii} \varphi_i^l = \varphi_i^{k+} [\mathbf{C}(t, \Phi\bar{\mathbf{u}})]_{ii} \varphi_i^k = \frac{|E_i|}{|\Omega_k|} [C_{11}(t, \Phi\bar{\mathbf{u}})]_{ii} = 0 \quad (52)$$

397 The matrix $[\Phi^+ \mathbf{C}(t, \Phi\bar{\mathbf{u}}) \Phi]_{kl} = 0$ for all $k, l = 1, 2, \dots, N$, and thus,

$$\bar{\mathbf{C}}(t, \bar{\mathbf{u}}) = \Phi^+ \mathbf{C}(t, \Phi\bar{\mathbf{u}}) \Phi = \mathbf{0} \quad (53)$$

398 as indicated by the LCM in eq. (9).

399 A.2.2 Magnitude Analysis for Residual Dynamics

400 Next, the magnitude of the residual dynamics $\mathbf{r}^{(2)}(\mathbf{u}, t)$ is analyzed to pinpoint the missing
 401 physics in the LCM. By definition,

$$\mathbf{r}^{(2)}(\mathbf{u}, t) = \dot{\bar{\mathbf{u}}} - \mathbf{r}^{(1)}(\bar{\mathbf{u}}, t) \quad (54a)$$

$$= \Phi^+ \mathbf{r}(\mathbf{u}, t) - \mathbf{r}^{(1)}(\mathbf{u}, t) \quad (54b)$$

$$\begin{aligned} &= \underbrace{\Phi^+ \mathbf{A}(\mathbf{u})^{-1} \mathbf{B}(\mathbf{u}) \mathbf{u} - \bar{\mathbf{A}}(\bar{\mathbf{u}})^{-1} \bar{\mathbf{B}}(\bar{\mathbf{u}}) \bar{\mathbf{u}}}_{\#1} + \underbrace{\Phi^+ \mathbf{A}(\mathbf{u})^{-1} \mathbf{C}(\mathbf{u}) \mathbf{u} - \bar{\mathbf{A}}(\bar{\mathbf{u}})^{-1} \bar{\mathbf{C}}(t, \bar{\mathbf{u}}) \bar{\mathbf{u}}}_{\#2} \\ &\quad + \underbrace{\Phi^+ \mathbf{A}(\mathbf{u})^{-1} \mathbf{f}(t) - \bar{\mathbf{A}}(\bar{\mathbf{u}})^{-1} \bar{\mathbf{f}}(t)}_{\#3} \end{aligned} \quad (54c)$$

402 The magnitude analysis for terms $\#1$ and $\#3$ can be found in Ref. [x](#). The analysis for term
 403 $\#2$ is presented next. Let $\mathbf{D}(\bar{\mathbf{u}}) = \mathbf{A}(\Phi\bar{\mathbf{u}})^{-1} \mathbf{P} \mathbf{C}(t, \Phi\bar{\mathbf{u}})$, then,

$$\Phi^+ \mathbf{A}(\mathbf{u})^{-1} \mathbf{C}(\mathbf{u}) \mathbf{u} - \bar{\mathbf{A}}(\bar{\mathbf{u}})^{-1} \bar{\mathbf{C}}(t, \bar{\mathbf{u}}) \bar{\mathbf{u}} \quad (55a)$$

$$= \Phi^+ \mathbf{A}(\mathbf{u})^{-1} \mathbf{C}(\mathbf{u}) \mathbf{u} - \Phi^+ \mathbf{A}(\Phi\bar{\mathbf{u}})^{-1} \mathbf{P} \mathbf{C}(t, \Phi\bar{\mathbf{u}}) \Phi \Phi^+ \mathbf{u} \quad (55b)$$

$$= \Phi^+ \mathbf{A}^{-1}(\mathbf{u}) \mathbf{C}(\mathbf{u}) \mathbf{u} - \Phi^+ \mathbf{D}(\bar{\mathbf{u}}) \Phi \Phi^+ \mathbf{u} \quad (55c)$$

$$(55d)$$

404 where $\mathbf{P} = \Phi\Phi^+$. Thus,

$$\|\Phi^+\mathbf{A}(\mathbf{u})^{-1}\mathbf{C}(\mathbf{u})\mathbf{u} - \bar{\mathbf{A}}^{-1}(\bar{\mathbf{u}})\bar{\mathbf{C}}(t, \bar{\mathbf{u}})\bar{\mathbf{u}}\| \quad (56a)$$

$$\leq \|\Phi^+\mathbf{A}^{-1}(\mathbf{u})\mathbf{C}(\mathbf{u})\mathbf{u} - \Phi^+\mathbf{D}(\bar{\mathbf{u}})\mathbf{u}\| + \|\Phi^+\mathbf{D}(\bar{\mathbf{u}})\mathbf{u} - \Phi^+\mathbf{D}(\bar{\mathbf{u}})\Phi\Phi^+\mathbf{u}\| \quad (56b)$$

$$\leq \|\Phi^+\| \underbrace{\|\mathbf{A}^{-1}(\mathbf{u})\mathbf{C}(\mathbf{u})\mathbf{u} - \mathbf{D}(\bar{\mathbf{u}})\mathbf{u}\|}_{\#1} + \|\Phi^+\mathbf{D}(\bar{\mathbf{u}})\| \underbrace{\|\mathbf{u} - \Phi\Phi^+\mathbf{u}\|}_{\#2} \quad (56c)$$

405 where term $\#2$ is due to the approximation of non-uniform temperature as constants, and
406 term $\#1$ is the error in the advection dynamics due to coarse-graining.

407 A.3 Lumped Capacitance Model

408 The following assumptions are employed: (1) the temperature in component (i) is described
409 by a scalar time-varying average temperature $\bar{u}^{(i)}$, (2) between neighboring components (i)
410 and (j) the heat flux is approximated as,

$$q_{ij} = \frac{\bar{u}^{(j)} - \bar{u}^{(i)}}{R_{ij}} \quad (57)$$

411 where R_{ij} is the thermal resistance. Empirically, for a component of isotropic heat conduction
412 with thermal conductivity k , length ℓ , and cross-section area A , the thermal resistance is $R = \ell/kA$. Between
413 components i and j , define $R_{ij} = R_i + R_j$. In addition, the heat flux due to Dirichlet
414 boundary condition is computed as $q_{iT} = (T_b - \bar{u}^{(i)})/R_i$.

415 At component i , the dynamics of LCM are given by,

$$\int_{E^{(i)}} \rho c_p \dot{\bar{u}}^{(i)} dE^{(i)} = \left(\sum_{j \in \mathcal{N}_i} \int_{e_{ij}} \frac{\bar{u}^{(j)} - \bar{u}^{(i)}}{R_{ij}} de_{ij} \right) + \int_{e_{iq}} q_b de_{iq} + \int_{e_{iT}} \frac{T_b - \bar{u}^{(i)}}{R_i} de_{iT} \quad (58a)$$

$$\bar{A}^{(i)} \dot{\bar{u}}^{(i)} = \left(\sum_{j \in \mathcal{N}_i} \frac{|e_{ij}|}{R_{ij}} (\bar{u}^{(j)} - \bar{u}^{(i)}) \right) + |e_{iq}| \bar{q}^{(i)} + \frac{|e_{iT}|}{R_i} (\bar{T}^{(i)} - \bar{u}^{(i)}) \quad (58b)$$

$$= \sum_{j \in \mathcal{N}_i} \left(-\frac{|e_{ij}|}{R_{ij}} \bar{u}^{(i)} + \frac{|e_{ij}|}{R_{ij}} \bar{u}^{(j)} \right) + \left(-\frac{|e_{iT}|}{R_i} \bar{u}^{(i)} \right) + \left(|e_{iq}| \bar{q}^{(i)} + \frac{|e_{iT}|}{R_i} \bar{T}^{(i)} \right) \quad (58c)$$

$$= \sum_{j \in \mathcal{N}_i \cup \{T_b\}} \left(\bar{B}_{ij}^{(i)} \bar{u}^{(i)} + \bar{B}_{ij}^{(j)} \bar{u}^{(j)} \right) + \bar{f}^{(i)} \quad (58d)$$

416 where in eq. (58b) $|e|$ denotes the length ($d = 2$) or area ($d = 3$) of a component boundary
417 e . The $\bar{A}^{(i)}$, $\bar{B}_{ij}^{(i)}$, and $\bar{B}_{ij}^{(j)}$ quantities are provided in eq. (12).

418 The lumped-mass representation for the four-component TPS is shown in Fig. 2. Let v_i

⁴¹⁹ represent the area of the i -th element, $\overline{\rho c_p}_i$, the heat capacity evaluated using the average
⁴²⁰ temperature $\bar{u}^{(i)}$, and $1/R_{ij} = 1/R_i(\bar{u}^{(i)}) + 1/R_j(\bar{u}^{(j)})$ the equivalent thermal resistance
⁴²¹ between elements i and j . Leveraging the formulas from eqs. (11) and (12), the LCM
⁴²² matrices are given by,

$$\bar{\mathbf{A}} = \begin{bmatrix} \overline{\rho c_p}_1 v_1 & 0 & 0 & 0 \\ 0 & \overline{\rho c_p}_2 v_2 & 0 & 0 \\ 0 & 0 & \overline{\rho c_p}_3 v_3 & 0 \\ 0 & 0 & 0 & \overline{\rho c_p}_4 v_4 \end{bmatrix}, \quad (59a)$$

$$\bar{\mathbf{B}} = \begin{bmatrix} \frac{1}{R_{12}} + \frac{1}{R_{14}} & -\frac{1}{R_{12}} & 0 & -\frac{1}{R_{14}} \\ -\frac{1}{R_{12}} & \frac{1}{R_{12}} + \frac{1}{R_{24}} + \frac{1}{R_{23}} & -\frac{1}{R_{23}} & -\frac{1}{R_{24}} \\ 0 & -\frac{1}{R_{32}} & \frac{1}{R_{32}} + \frac{1}{R_{34}} & -\frac{1}{R_{34}} \\ -\frac{1}{R_{14}} & -\frac{1}{R_{24}} & -\frac{1}{R_{34}} & \frac{1}{R_{14}} + \frac{1}{R_{24}} + \frac{1}{R_{34}} \end{bmatrix}, \quad \bar{\mathbf{f}} = \begin{bmatrix} \bar{q}^{(1)} \\ \bar{q}^{(2)} \\ \bar{q}^{(3)} \\ 0 \end{bmatrix} \quad (59b)$$

⁴²³ References

- ⁴²⁴ [1] Adam J. Amar, A. Brandon Oliver, Benjamin S. Kirk, Giovanni Salazar, and Justin Dobra. Overview of the charring ablator response (char) code. In AIAA, editor, *AIAA Aviation Forum*, 2016.
- ⁴²⁷ [2] Guy L. Bergel, Frank B. Beckwith, Gabriel J. de Frias, Kevin M. Manktelow, Mark T. Merewether, Scott T. Miller, Krishen J. Parmar, Timothy S. Shelton, Jesse T. Thomas, Jeremy T. Trageser, Benjamin T. Treweek, Michael V. Veilleux, and Ellen B. Wagman. *Sierra/SolidMechanics 5.6 User's Manual*, 2022.
- ⁴³¹ [3] Gary Cohen and Sébastien Pernet. *Finite Element and Discontinuous Galerkin Methods for Transient Wave Equations*. Springer Dordrecht, Le Chesnay and Toulouse France, 2018.
- ⁴³⁴ [4] Frank P. Incropera, David P. DeWitt, Theodore L. Bergman, and Adrienne S. Lavine. *Fundamentals of Heat and Mass Transfer*. Wiley, Hoboken, NJ, 7th edition, 2011.